Article

Molecular mechanism of thyroxine transport by monocarboxylate transporters

Matteo Tassinari[1], Giorgia Tanzi [1], Francesco Maggiore [1], Stefan Groeneweg[2], Ferdy S. van Geest [2], Matthijs E. T. Freund [2], Christiaan J. Stavast [2], Irene Boniardi [1], Sebastiano Pasqualato [1], W. Edward Visser [2] ✉ & Francesca Coscia [1] ✉

Thyroid hormones (the common name for prohormone thyroxine and the bioactive form triiodothyronine) control major developmental and metabolic processes. Release of thyroid hormones from the thyroid gland into the bloodstream and their transport into target cells is facilitated by plasma membrane transporters, including monocarboxylate transporter (MCT)8 and the highly homologous MCT10. However, the molecular mechanism underlying thyroid hormone transport is unknown. The relevance of such transporters is illustrated in patients with MCT8 deficiency, a severe neurodevelopmental and metabolic disorder. Using cryogenic-sample electron microscopy (cryo-EM), we determined the ligand-free and thyroxine-bound human MCT8 structures in the outward-facing state and the thyroxine-bound human MCT10 in the inward-facing state. Our structural analysis revealed a network of conserved gate residues involved in conformational changes upon thyroxine binding, triggering ligand release in the opposite compartment. We then determined the structure of a folded but inactive patient-derived MCT8 mutant, indicating a subtle conformational change which explains its reduced transport activity. Finally, we report a structure of MCT8 bound to its inhibitor silychristin, locked in the outward-facing state, revealing the molecular basis of its action and specificity. Taken together, this study advances mechanistic understanding of normal and disordered thyroid hormone transport.

Thyroid hormones, including the prohormone T4 (3,3',5,5'-tetraiodo-L-thyronine or thyroxine) and the bioactive T3 (3,3',5-triiodo-L-thyronine)[1,2] are critical for normal development and metabolism in all cells[3]. Plasma membrane transporters facilitate the transfer of thyroid hormones across the plasma membrane, thereby critically governing intracellular thyroid hormone concentrations[4,5].
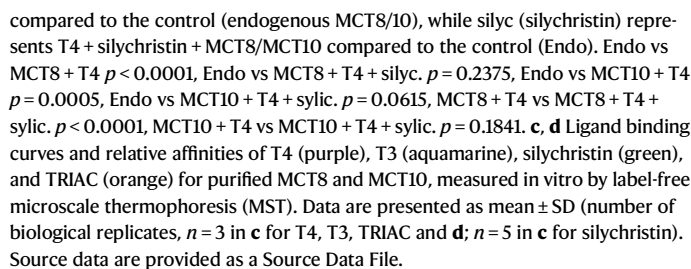
Monocarboxylate transporter (MCT)8 is the most specific thyroid hormone transporter and facilitates the release of thyroid hormones from the thyroid and into neuronal cells and other cell types[4]. Loss-of-function (LoF) mutations in the X-chromosomal *SLC16A2* gene, encoding MCT8, cause severe intellectual and motor disability due to cerebral hypothyroidism and clinical features such as underweight and tachycardia secondary to chronic peripheral thyrotoxicosis, with ~30% dying in childhood[6]. Survival rate and the severity of disease features are strongly determined by the functional impact of the LoF mutations[7]. Treatment with the T3 analog 3,5,3'-triiodothyroacetic acid (TRIAC), which is able to enter cells independently from MCT8, alleviates peripheral thyrotoxicosis features[8,9]. Among MCTs, MCT10 is

[1]Human Technopole, Milano, Italy. [2]Department of Internal Medicine, Academic Centre for Thyroid Diseases, Erasmus Medical Centre, Rotterdam, The Netherlands. ✉e-mail: w.e.visser@erasmusmc.nl; francesca.coscia@fht.org

the most similar to MCT8, with 49% sequence identity and the only other thyroid hormone transporter in this protein family[10]. Both are capable of transporting thyroid hormones in a sodium-independent manner, with MCT10 also being able to translocate aromatic amino acids[2]. However, the physiological function of MCT10 is currently unclear, and it is unable to compensate for loss of MCT8 function[4]. In vitro, the flavonolignan silychristin specifically inhibits MCT8[2,11], but not MCT10[2,12]. Despite the central role of these plasma membrane transporters, the molecular details of substrate binding and transport mechanisms have been elusive[11,13].

Here, utilizing cryogenic-sample electron microscopy (cryo-EM), we determined five structures describing different states of the thyroxine transport cycle: human MCT8 in the ligand-free, thyroxine-bound, silychristin-bound, a patient-derived D424N mutant (D498 in the long isoform, see Supplementary Fig. 10) in the outward-facing state (OFS), and the thyroxine-bound human MCT10 in the inward-facing state (IFS). Our structural study, combined with biophysics binding and cellular transport assays, provides insights into the

mechanisms of action of these two homologous thyroid hormone transporters[10].

Results

Thyroid hormone binding and transport

To study thyroid hormone binding and transport, we genetically fused an N-terminal FLAG tag to both targets. First, we verified that upon overexpression of FLAG-MCT8 and FLAG-MCT10 (Fig. 1a, b) in HeLa cells, T4 added in the cellular medium is efficiently transported. The addition of the inhibitor silychristin clearly reduces MCT8-mediated transport (Fig. 1a, b), confirming its inhibitory action on the transporter[12]. In the case of MCT10, we observe a trend for a non-inhibitory effect on T4 transport, in line with previous reports[12].

We then isolated and overexpressed FLAG-MCT8 and FLAG-MCT10 in detergent, which were purified as a monodisperse peak in size-exclusion chromatography (Supplementary Fig. 1a, b). Although higher order species are visible by SDS-PAGE and western blot analysis (Supplementary Fig. 1c, d), both proteins are monomeric and well-

Fig. 1 | T4 transport and its inhibition by silychristin in MCT8 and MCT10.
a Representative confocal images of immunofluorescence experiments: intracellular T4 and FLAG (MCT8 or MCT10) were detected in HeLa cells overexpressing FLAG-MCT8 and FLAG-MCT10 exposed to 10 μM T4, in absence or in presence of 10 μM silychristin. **b** Quantification of T4 uptake by HeLa cells overexpressing FLAG-MCT8 or FLAG-MCT10. Data are presented as mean values ± SD (number of biological replicates $n = 4$ for endogenous protein levels (Endo), $n = 4$ for MCT10, $n = 3$ for MCT8). The normalization was performed on overexpressed MCT8 + T4 HeLa cells. P values are based on ordinary one-way ANOVA (****$p < 0.0001$, ***$p = 0.0005$, ns > 0.05). In the legend, T4 represents T4 + MCT8 and T4 + MCT10

compared to the control (endogenous MCT8/10), while silyc (silychristin) represents T4 + silychristin + MCT8/MCT10 compared to the control (Endo). Endo vs MCT8 + T4 $p < 0.0001$, Endo vs MCT8 + T4 + silyc. $p = 0.2375$, Endo vs MCT10 + T4 $p = 0.0005$, Endo vs MCT10 + T4 + sylic. $p = 0.0615$, MCT8 + T4 vs MCT8 + T4 + sylic. $p < 0.0001$, MCT10 + T4 vs MCT10 + T4 + sylic. $p = 0.1841$. **c, d** Ligand binding curves and relative affinities of T4 (purple), T3 (aquamarine), silychristin (green), and TRIAC (orange) for purified MCT8 and MCT10, measured in vitro by label-free microscale thermophoresis (MST). Data are presented as mean ± SD (number of biological replicates, $n = 3$ in **c** for T4, T3, TRIAC and **d**; $n = 5$ in **c** for silychristin). Source data are provided as a Source Data File.

folded, as also judged by preliminary cryo-EM analysis (Supplementary Fig. 1e, f).

We measured the affinity of purified MCT8 and MCT10 for thyroid hormones in vitro, using label-free microscale thermophoresis (MST) (Fig. 1c, d and Supplementary Fig. 2b). FLAG-MCT8 showed a K_d of 8.9 μM for T4, of 25.2 μM for T3 and 56.9 nM for silychristin, the latter being confirmed by isothermal titration calorimetry (ITC) measuring a K_d of 44.5 nM (Supplementary Fig. 2a). FLAG-MCT10 showed a K_d of 8.9 μM for T4, of 10.7 μM for T3, while binding to silychristin was beyond 75 μM. In addition, we measured a 20 μM and 19 μM affinity for TRIAC binding to MCT8 and MCT10, respectively (Fig. 1c, d). These biophysical and cellular data are in line with previous reports[1,2,4] and confirm preserved activity and ligand binding properties of the purified recombinant FLAG-tagged MCT constructs.

Structures of MCT8 and MCT10 along the T4 transport cycle

In the present study, we numbered the residues according to the short MCT8 isoform (Uniprot ID: P36021); to convert the number to the long MCT8 isoform NP_006508.1 (which has been used until now to describe patient mutations and in homology models), 74 amino acids should be added (Supplementary Fig. 10). Our first attempts for structural characterization of MCT8 and MCT10 by cryo-EM, both in detergents and amphipols, were not successful as we obtained low-resolution reconstructions or severe preferred orientation within the EM grid, precluding accurate substrate and protein model building. We then engineered both MCT8 and MCT10 with a C-terminal ALFA tag (see construct details in the methods section and Supplementary Fig. 10) and reconstituted a complex with an anti-ALFA nanobody (NbALFA, as described in Fig. 2a) and in presence of amphipols (Supplementary Fig. 3). This strategy considerably improved the orientation distribution and angle assignment accuracy (Supplementary Fig. 4), enabling us to obtain cryo-EM maps of the ligand-free MCT8 in the OFS, T4-bound MCT8 in the OFS and of T4-bound MCT10 in the IFS at the resolutions of 3.5 Å, 3.4 Å and 3.8 Å, respectively (Fig. 2b, c, e). Both MCT8 and MCT10 display the classical bilobed architecture of the major facilitator superfamily, including an N-terminal domain (NTD) formed by transmembrane helices (TMH) 1–6 and a C-terminal domain (CTD) formed by TMH7–12[14–16]. Extradensities for the ligand T4 are visible in cryo-EM maps of both MCT8 and MCT10 (Fig. 2d, f and Supplementary Fig. 5). In all structures of MCT8, the CTD residues facing the solvent-exposed central protein gate Y339 (TMH7) and R371 (TMH8) are linked via an H-bond and a salt bridge through D424 (TMH10) (Supplementary Fig. 6a). The MCT8 pocket accommodates the two iodinated aromatic rings of T4 in an inner highly hydrophobic pocket, while the amino acidic moiety is positioned towards the outward wide opening (Fig. 2h). The T4 carboxylic group is bound via a salt bridge to R371 which reorients towards it with respect to the ligand-free structure (Fig. 2g, h). We believe that the presence of the T4 carboxylic group partially destabilizes the CTD network (D424N bridging R371 and Y339). The T4 amino group of the substrate points towards N119 on the NTD lobe, although it does not appear to establish direct interactions with the hormone (the N119-Cβ to T4-N distance is ~6 Å). Overall, the ligand-free and T4-bound MCT8 structures appear almost identical (RMSD 1.018 Å), but we observe a subtle conformational change where the TMH7 kinks. In particular, the F336-Y335 pair moves closer to the substrate, causing Y339 (along the same TMH7) to approach N119 (Cα-Cα distance from 13.8 to 11.2 Å) on the opposite NTD lobe, thereby partially occluding the gate (Fig. 2g, h, j, k). In the T4-bound MCT10 structure (IFS), the CTD is stabilized by the same interactions as in MCT8 (Y311 on TMH7 is held to R343 on TMH8 via D396 on TMH10) (Supplementary Fig. 6b). T4 appears rotated with respect to MCT8, but the carboxylic group is still tightly coordinated by the R343 (R371 in MCT8). The Y311-N89 pair (Y339-N119 in MCT8) seals the gate (Cα-Cα distance 6.4 Å) on the outward-facing compartment, and T4 becomes accessible to the opposite compartment, where it is conveyed by concentration gradient (Fig. 2i, l).

Overall, the comparison among the structures of the highly conserved transporters in the OFS and IFS suggests that the transport of T4 in both MCT transporters is initiated upon sensing of the substrate, mostly on the CTD lobe. The latter lobe is tightly held together by the central residue D424, allowing a concerted closure of CTD and NTD close to the amino acidic group of T4. To corroborate these observations, we measured the affinity for T4 and transport efficiency of MCT8 (and corresponding MCT10) variants in which we mutated residues participating in the binding to the hydrophobic moiety of T4 (F115) and to the amino acid group (R371, N119), F336 involved in the transition from OFS to IFS (Fig. 2m–o) and D424 stabilizing the CTD (Supplementary Fig. 6a). Intriguingly, none of the single residues is essential for substrate binding, but mutation of N119, D424 and R371 (conserved in MCT10) severely reduced T4 transport, i.e., these residues are crucial for the transition from OFS to IFS (Fig. 2o). In conclusion, the comparison between these three structures allowed us to identify a set of key residues involved in a common mechanism of thyroxine transport by MCT8 and MCT10. Our findings are also in agreement with previous functional studies on the conserved R371[17].

Structure of the MCT8 pathogenic variant D424N

Structural analysis of MCT8 and MCT10 in the presence of T4 highlighted that D424 is a key residue not directly involved in substrate binding, but essential for transport. Indeed, the patient-derived mutation c.1492G > A corresponds to the D424N variant, associated with clinical features at the severe end of the phenotypic spectrum of MCT8 deficiency[18]. To understand why this isosteric mutation affects T4 transport and to support the hypothesized mechanism of MCT8 action, we determined the architecture of MCT8 D424N mutant by cryo-EM, obtaining a map at an overall resolution of 4.0 Å (Fig. 3a, b). When we first approached structural characterization of MCT8 D424N we engineered an ALFA tag at residue 505 as for WT MCT8, however obtaining a very poor nanobody binding (Supplementary Fig. 3c). We believed this was due to the protein inherent flexibility or a different conformation and repositioned the tag at residue 512, further away on the same protein lobe (Supplementary Fig. 10). The protein looked still well folded and could properly bind the NbALFA (Supplementary Fig. 3b). This tag repositioning helped structure determination, despite the nanobody being averaged out in our reconstruction due to a larger distance from the transmembrane moiety. Our model shows that the MCT8 D424N protein variant is in the OFS, with an overall folding similar to ligand-free MCT8 (RMSD 1.8 Å). Referring to the main chain, in MCT8 D424N, while the NTD remains basically unaltered, within the CTD TMH7 and TMH10 are shifted away from the central gate axis by a consequence of the weaker bond between Y339 and N424 (Fig. 3c, d). Due to the destabilization of the CTD, with respect to ligand-free WT MCT8, in the D424N mutant, the Cα of Y339 is shifted by 2.1 Å, and the gate widening at the level of the mutation is increased by about 1 Å (Y339-N119 Cα-Cα changes from 13.9 to 14.9 Å). This shift is propagated along the helix towards the outward opening by about 5 Å (Cα-Cα Y125-H341 on TMH7 increasing from 18.1 to 23.2 Å) (Fig. 3c, d). Overall, the model and map suggest an increased flexibility of CTD and, on average, a wider opening of the outward-facing lobes (Fig. 3c, d).

As measured by MST and by visual inspection of the ligand binding pocket, the protein is still competent for T4 binding (Fig. 2m). Nevertheless, we infer that the absence of the crucial D424, which holds together the CTD, hampers an efficient TMH7-initiated movement, required for the concerted conformational change from the OFS to the IFS. In conclusion, the structure of the pathogenic MCT8 D424N mutant confirms the mechanism of thyroid hormone transport derived by the WT structures and suggests a rationale for its defective activity.
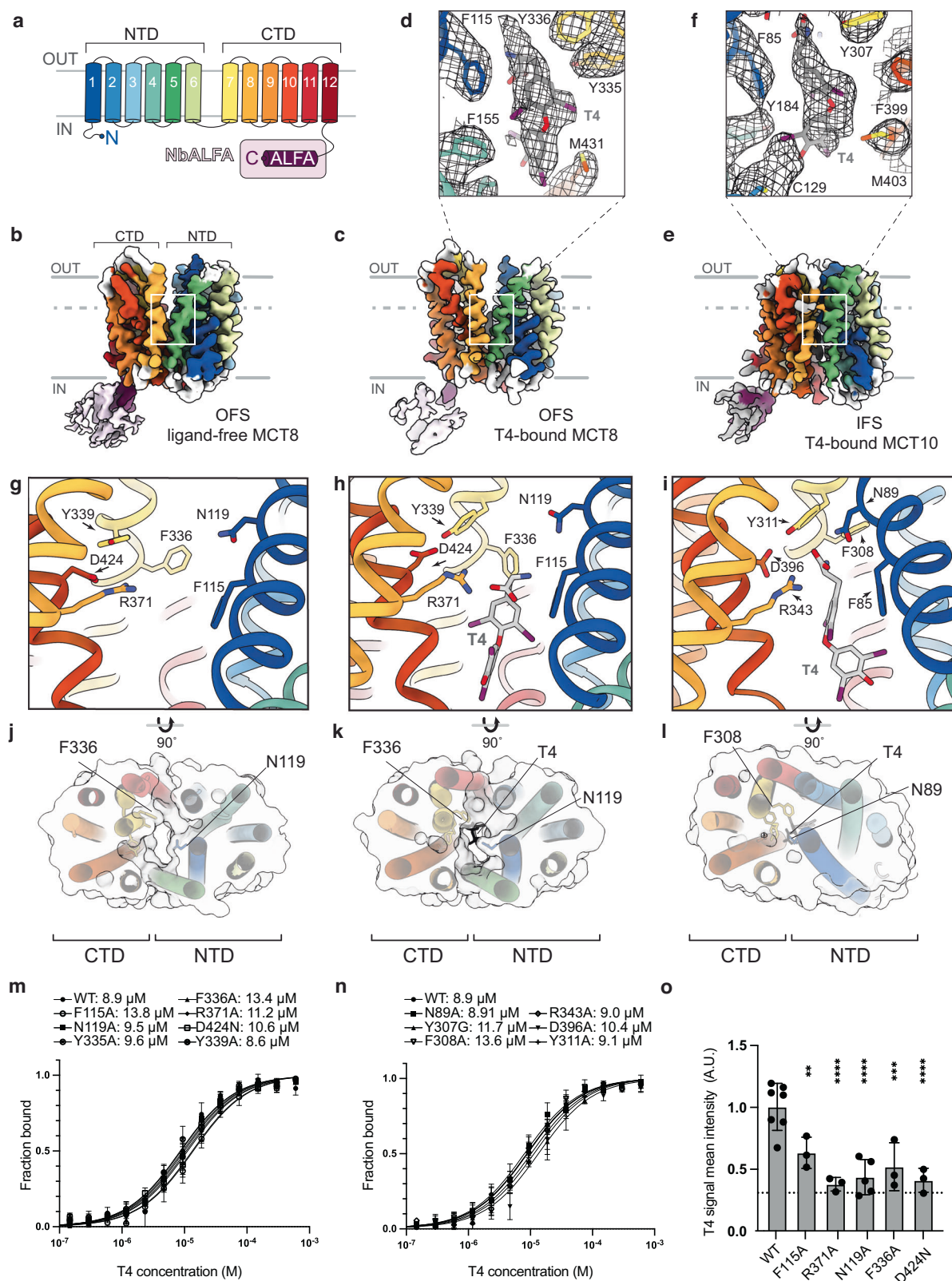
Mechanism of MCT8 inhibition by silychristin

Having derived a mechanism of transport of T4 in MCT8 and MCT10, we set out to investigate the mechanism of inhibition of MCT8 by determining its cryo-EM structure in complex with its highly specific inhibitor silychristin (Fig. 4a–c). Our 3.0 Å resolution cryo-EM map allowed us to identify the binding pocket for the ligand within an OFS (Fig. 4a, b, Supplementary Fig. 5).

structures bound to the inhibitor and to T4 revealed that silychristin is located in the same binding pocket of T4, but it is shifted towards the outward compartment with respect to the thyroid hormone, and its three aromatic moieties do not coincide with the iodophenol rings of T4 (Fig. 4c). Indeed, T4 is more deeply embedded within the ligand gate, burying 93% of its solvent-accessible area (539 Å² of buried surface area out of 582 Å² accessible), locked by F336 upon local

Fig. 2 | Cryo-EM structures of MCT8 and MCT10. a Schematic representation of MCT transmembrane α-helices 1–6 (N-terminal domain, NTD) and 7–12 (C-terminal domain, CTD). The construct was engineered with an ALFA tag at the C-terminus to form a complex with its cognate nanobody NbALFA. Cryo-EM map of **b** ligand-free MCT8 in the outward-facing state (OFS), **c** T4-bound MCT8 in the outward-facing state (OFS), **d** T4-bound MCT10 in the inward-facing state (IFS). **d, f** Closed-up view on T4 binding site with the corresponding cryo-EM density for MCT8 and MCT10, respectively. **g–i** Zoomed views on the central gate region (corresponding to the white square in **b, c, e**), highlighting residues coordinating T4. **j–l** Cross sections of the surface of transporters (dotted line in **b, c, e**) indicating progressive closure of the gate, moving solvent accessibility of the substrate from the OUT to the IN compartment. To derive the position of residues in the long isoform of MCT8, 74 amino acids should be added (Supplementary Fig. 10). **m** T4 binding curves relative to MCT8 and its mutants measured by MST **n** T4 binding curves relative to MCT10 and its mutants measured by MST. Data are presented as mean ± SD (number of biological replicates, $n = 4$ in **m** with D424N, F336A, and in **n** with D396A; $n = 3$ for all the other samples). **o** Quantification of T4 uptake by HeLa cells overexpressing FLAG-MCT8 and its mutants (Supplementary Fig. 8). Data are presented as mean values ± SD (number of biological replicates, $n = 7$ with WT, $n = 5$ with N119A, and $n = 3$ for all the other samples). The dotted line indicates negligible endogenous MCT8 levels. Normalization was performed on overexpressed MCT8 + T4. P values are based on ordinary one-way ANOVA (**$p = 0.0091$, ***$p = 0.0007$, ****$p < 0.0001$). For the MCT8 mutants F115A $p = 0.0091$, R371A $p < 0.0001$, N119A $p < 0.0001$, F336A $p = 0.0007$, D424N $p < 0.0001$. Source data are provided as a Source Data File.
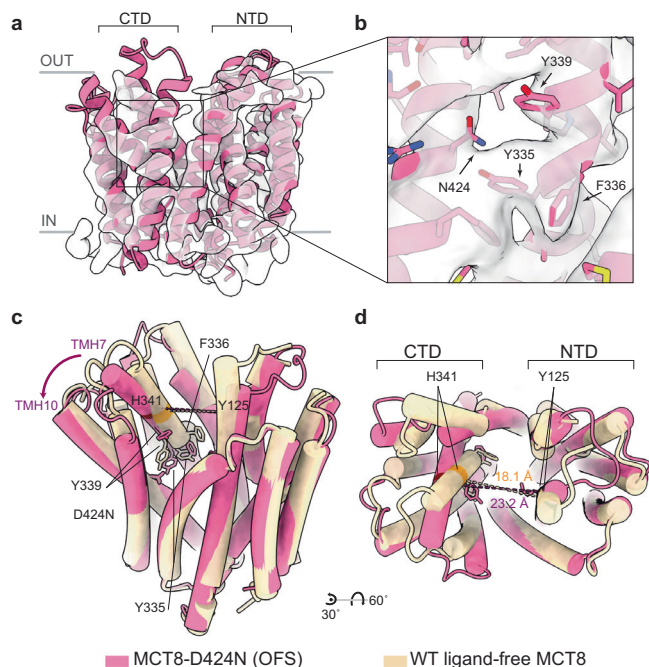
Fig. 3 | Structure of the patient-derived variant MCT8 D424N. a cryo-EM map of MCT8 D424N (D498N in the long isoform) corresponding to an outward-facing state (OFS). **b** cryo-EM map ($\sigma = 6.5$) close-up showing local density for D424N, Y335, Y339 and F336, and surrounding residues. **c, d** Overlap between ligand-free WT MCT8 and MCT8 D424N (D498N), showing larger flexibility and lateral shift in TMH7, which is more loosely held to TMH10 by a weaker Y339-N424 (Y413-N498) interaction. The distance between the two lobes, as measured from the distance Cα-Cα of H341-Y125, increases from 18.1 Å (WT) to 23.2 Å (D424N mutant). To derive the position of residues in the long isoform of MCT8, 74 amino acids should be added (Supplementary Fig. 10).

movement of TMH8. In contrast, silychristin buries only 85% of its solvent-accessible area (602 Å^2 of buried surface area out of 707 Å^2 accessible) and its binding does not imply significant conformational changes with respect to ligand-free MCT8 (RMSD = 1.051 Å). Our structural analysis suggests that the inhibitory effect of silychristin is exerted by the close interactions with F336, R371 within the CTD and F115, N119 on the opposite NTD lobe. Therefore, silychristin competes with T4 and stabilizes MCT8 in an apo-like conformation in which the protein is unable to undergo the conformational changes necessary for the transport (Fig. 4f). To validate this hypothesis, we performed MCT8 site-directed mutagenesis and measured the effects on both silychristin binding in vitro and its ability to inhibit T4 transport in cells (Fig. 4d, f). Our data show that F115A abolishes binding and, hence, inhibition by silychristin in MCT8. MCT8 mutants R371A and F336A can still partially bind silychristin, but T4 transport is no longer inhibited by

the binding of silychristin. A similar effect on silychristin binding is observed by preincubating MCT8 with 100 μM T4, indicating that when the hormone occupies the gate first by partially occluding it, the inhibitor can no longer efficiently compete with its binding in vitro. In addition, we performed a competitive T4 binding experiment in the presence of a large excess of silychristin. If the inhibitor first occupies the gate, T4 affinity decreases from 8.9 to 20.6 μM (about 65%), but hormone binding is not entirely abolished. While these data are consistent with a single MCT8 binding site that accommodates either one ligand or the other, silychristin may have a faster k_{off} rate compared to T4, allowing the hormone to outcompete silychristin partially. This hypothesis could also explain why the presence of T4 in the in vitro competition assay is able to induce an ~3000-fold reduction in silychristin binding affinity, despite it being a high-affinity ligand. This is in line with the fact that silychristin does not induce a partially occluded conformation in MCT8. Nevertheless, in cellular uptake assays, in the presence of silychristin, MCT8 is unable to transport T4, as the residue N119 is locked by direct interaction with the inhibitor and unable to reach the opposite Y339 on the CTD to close the gate in an IFS. In conclusion, our structural and functional data on the MCT8-silychristin complex indicate that the inhibitor does not entirely prevent thyroid hormone binding, but abolishes MCT8-mediated T4 transport by keeping the protein in an OFS, in agreement with previous reports[12]. Finally, we asked why T4 transport by MCT10 is not as strongly inhibited by silychristin as in MCT8, given the large number of conserved residues in the protein gate (Fig. 1b, Supplementary Fig. 7b). By overlapping the structure of MCT8-silychristin and the simulated OFS for MCT10 (derived in swiss-model[19]), we noticed that Y184 (F213 in MCT8) would produce a steric clash with silychristin (Fig. 4g, h), likely precluding a tight binding to the inhibitor. To verify this hypothesis, we measured both T4 uptake and its inhibition by silychristin relative to the MCT10 Y184F mutant (Fig. 4i and Supplementary Fig. 8). Indeed, MCT10 Y184F exerted an MCT8-like behavior in both T4 uptake and inhibition (a gain of function). We infer that this subtle amino acidic change enlarges the MCT10 binding pocket, allowing it to accommodate both T4 and silychristin better, and loosening specificity for smaller aromatic amino acidic ligands. These data are in agreement with previous studies on MCT10 variants[20].

Discussion

Thyroid hormone transporters are cellular gatekeepers for the regulation of intracellular thyroid hormone concentrations, orchestrating developmental and metabolic events in many tissues. In this work, upon engineering with an N-terminal FLAG and C-terminal ALFA tag, accompanied by binding to NbALFA, we determined five cryo-EM structures of human MCT8 and MCT10 as exemplary thyroid hormone transporters. In addition, we combined biophysical and functional studies to dissect the binding and mechanism of transport of thyroid hormone, as well as the molecular basis of its inhibition by silychristin.

A key finding suggested by our structures of MCT8 was that, upon substrate binding, a subtle conformational change in TMH7 (F336-
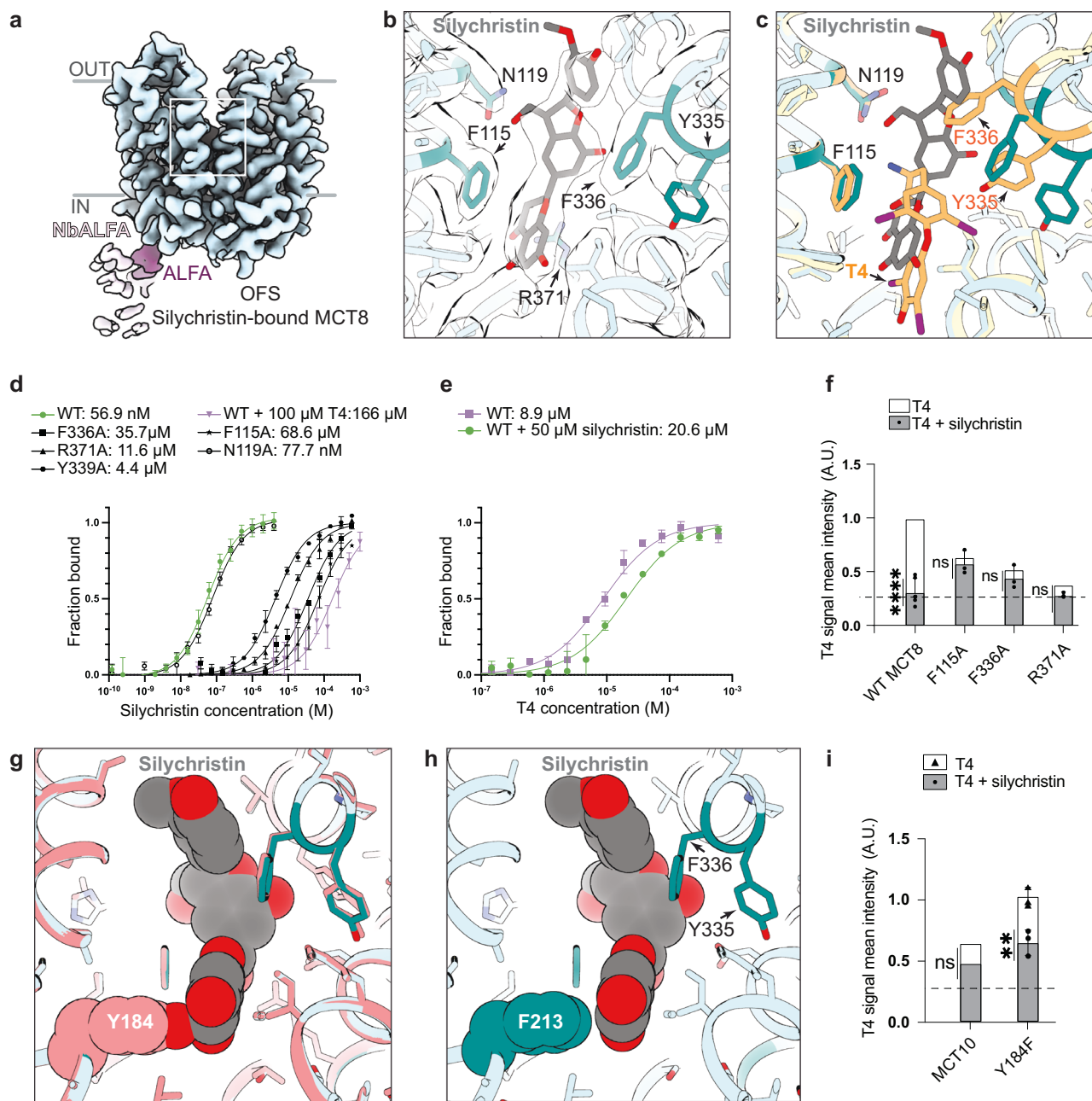
Fig. 4 | Structure of MCT8 bound to its inhibitor silychristin. a cryo-EM map of silychristin-bound MCT8 in the outward-facing state (OFS). **b** Close-up view on the ligand binding site with the corresponding cryo-EM density in white, showing interaction with T4 binding residues and T4 transport residues, F336, N119, F115, R371. **c** Overlap between T4-bound (pale yellow/gold) and silychristin-bound (pale cyan/teal) MCT8 in the OFS, showing that silychristin (gray) locks the protein in the OFS, preventing movement of F336 and N119 necessary for T4 transport.
d Silychristin binding curves of WT MCT8 (green), mutants (black), and WT pre-incubated with T4 (violet), obtained by MST. The curves show that the inhibitor binding is reduced when mutating F336 and R371 and Y339, or when the gate is already occupied by T4, but not when modifying N119. Data are presented as mean ± SD; $n = 4$ with silychristin, $n = 3$ for all the other samples. **e** MCT8-T4 binding profile (MST) of the sample was preincubated with 50 μM silychristin, showing reduced ability to bind the natural substrate in the presence of the inhibitor (green) compared to the control (violet). Data are presented as mean ± SD; $n = 3$.
f Quantification of T4 uptake by HeLa cells overexpressing FLAG-MCT8 and its mutants (Supplementary Fig. 8). Data are presented as mean values ± SD (number

of biological replicates, $n = 6$ for WT, and $n = 3$ for all the other samples). Data are normalized on MCT8 WT + T4. The dotted line indicates negligible T4 uptake by untreated HeLa. P values based on ordinary one-way ANOVA (****$p < 0.0001$ for MCT8 WT + T4 vs MCT8 WT + T4 + silychristin, and for all the mutants + T4 vs mutants + T4 + silychristin $p > 0.9999$ (ns)). **g** Simulated MCT10 OFS structure in complex with silychristin, showing a steric clash between Y184 and the inhibitor. **h** MCT8-silychristin structure showing lack of steric clash between F213 (Y184 in MCT10) and the inhibitor. **i** Quantification of T4 uptake by HeLa cells over-expressing FLAG-MCT10 and its mutant Y184F (Supplementary Fig. 8). Data are presented as mean values ± SD (number of biological replicates, $n = 4$ with MCT10 WT, and $n = 3$ for MCT10 Y184F). The dotted line indicates negligible T4 uptake by untreated HeLa. Data are normalized on MCT8 WT + T4 as shown in Fig. 1b. P values based on ordinary one-way ANOVA (MCT10 WT + T4 vs MCT10 WT + T4 + silychristin $p = 0.1778$, MCT10 Y184F + T4 vs MCT10 Y184F + T4 + silychristin $p = 0.0028$ (**)). To derive the position of residues in the long isoform of MCT8, 74 amino acids should be added (Supplementary Fig. 10). Source data are provided as a Source Data File.
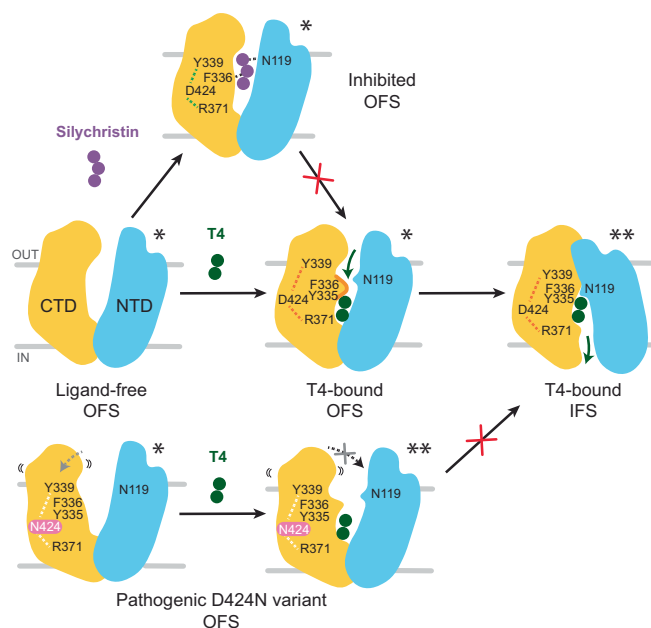
Fig. 5 | Proposed model of the mechanism of MCT8-mediated thyroxine (T4) transport and of its inhibition. Schematic illustration of MCT8 conformations during the thyroid hormone transport cycle. The states marked with * represent experimentally obtained conformations in this study, while ** were inferred by homology modeling and supported by our assays. The T4-bound IFS cartoon was derived from the structure of T4-bound MCT10, determined in this work. MCT8 D424N binds but does not transport T4, as shown by in vitro binding and *in cellulo* T4 uptake assays. To derive the position of residues in the long isoform of MCT8, 74 amino acids should be added (Supplementary Fig. 10).

Y339) initiates a continuous movement of CTD TMHs, stabilized by the pivotal residue D424. Hence, Y339 progressively approaches N119 on the opposite NTD lobe, closing the gate. T4 is then exposed to the opposite membrane compartment for release (Fig. 5 and Supplementary Movie 1). T4 is tightly bound to MCT8 via both hydrophobic interactions coordinating its aromatic moieties and via electrostatic interaction between the carboxylate within the amino acidic group and R371, highly conserved in the MCTs family (Supplementary Fig. 7b).

The bioactive hormone T3 (bearing a mono-iodinated phenol ring) binds with lower affinity to MCT8 (Fig. 1c), but shows a comparable transport efficiency as T4[1,21]. We hypothesize that differential binding and transport of these very similar hormones is due to higher retention of T4 in the binding pocket, given its larger binding surface, which is then less efficiently released by the protein upon exposure to the gradient concentration.

Our data and previous reports have highlighted that the T3 analog TRIAC (bearing the same T3 aromatic moiety, but lacking the amino group) binds MCT8 (and MCT10) with an affinity similar to T3, yet it is not transported by MCT8[22] (Fig. 1c). Hence, TRIAC could potentially act as a mild inhibitor of MCT8, in line with cis-inhibitory studies showing that TRIAC inhibits MCT8-mediated T3 transport[21]. At the same time, di-iodo-tyrosine (DIT), lacking half of the aromatic moiety (one di-iodo-ring with respect to T4), is transported by MCT8[23]. These data suggest that the amino group of the ligand plays a crucial role in the transport mechanism, but not in the ligand binding.

By overlapping the T4-bound MCT8 and MCT10 structures (Supplementary Fig. 6b) we observe that upon conformational change to the IFS, F115 (F85 in MCT10) comes closer to the T4 amino group (with Cβ in F115−N in T4 going from 4.2 to 2.8 Å). Possibly, a repulsion between F115 and the amino group causes the relocation of the hormone in the gate from its original engagement position in the OFS (Supplementary Fig. 6b). In the new IFS T4 position we observe that

some contacts are loosened (e.g., the distance between I3′ and Cε of Met 431/403 increase from 3.9 to 6.5 Å). Hence, we propose that the T4 amino group is a pivot point to facilitate hormone release in the IFS. In the absence of the amino group in the ligand (e.g., for TRIAC), we infer that the protein would still be able to undergo an OFS to IFS conformational change, but without destabilizing the ligand binding, thereby probably preventing its release.

These hypotheses are supported by the fact that F115A and N119A reduce transport but not binding of T4 (Fig. 2m−o); nevertheless, more structural information about other states of MCT8/10 would be necessary to corroborate them further. Previous studies suggested an important role for H118 in substrate binding[11,24]. Here, we observe that the H118 side chain is indeed exposed to the solvent and is thus available for chemical modification by His-reactive diethyl pyrocarbonate, but does not directly interact with T4 in the currently determined conformational states.

Leveraging the structural information obtained in this work, we sought to understand what makes MCT8 and 10 specifically conveying thyroid hormone with respect to the other members of the family of MCTs[10] and if a common transport mechanism exists.

By comparing the structures of MCT8-T4 and MCT1 in the OFS bound to its substrate lactate[25] (PDB ID 6LZ0), we observe that the carboxylic group is in a similar position with respect to the lactate coordinated by the residue R371 (R313 in MCT1), highly conserved within the MCT family (Supplementary Fig. 7a, b). Therefore, ligand sensing occurs via a similar electrostatic interaction in MCTs (Supplementary Fig. 7a), in accordance with previously reported homology models[12,13] and chemical modification studies[11,13,17]. However, the MCT1 lactate binding pocket is much smaller, shaped by large hydrophobic residues which hamper thyroid hormone accommodation in the gate; the critical transport MCT8 residue N119 corresponds to a longer K38, which in MCT8 would clash with the amino group of T4 or other amino acids, preventing their binding (Supplementary Fig. 7a). Therefore, MCT1 gate is likely incompatible with amino acidic binding (and thus transport).

Regarding residues involved specifically in the T4 transport, rather than binding, we noticed that the Y339 and D424 pair is exclusively present in the thyroid hormone transporters MCT8 and MCT10 (Supplementary Fig. 7b)[11]. In MCT1, the residue D309, driving proton-coupled transport, corresponds to a serine (S367 in MCT8), while D424 corresponds to a F367 (Supplementary Fig. 7a). Based on this comparison, we surmise that the overall mechanism of ligand transport is different in MCT1 and MCT8/10.

On the other hand, considering the canonical amino acid transporter LAT1 structure bound to DIT (PDB ID 7DSQ)[26], both the amino and carboxylic groups are mostly coordinated by backbone interactions rather than by side chains. Therefore, despite the shared nature of the ligands, as the sequence identity between LAT1 and MCT8/10 is overall poor, the mechanisms of binding and transport seem different in the two protein families.

In this work, we also revealed the molecular basis of specific inhibition of MCT8 by silychristin, which we show coordinating both the NTD and CTD of MCT8 stalling it in an OFS (Fig. 4). Our binding studies indicate that T4 is still weakly binding MCT8 in presence of silychristin, but its transport can no longer occur given the large number of interactions of the inhibitor, with a K_d considerably lower with respect to T4. Moreover, we structurally identified that Y184 represents a minor but key difference in the MCT10 gate with respect to the F213 in MCT8 (Fig. 4g−i). Indeed, the MCT10 Y184F mutant shows an increased T4 uptake in cells and becomes more sensitive to inhibition by silychristin, in line with previous biochemical observations[20].

Finally, we aimed at providing insights into a disease mechanism in MCT8, whose deficiency is associated with severe neurodevelopmental and metabolic problems. We studied the structure and

function of the MCT8 patient-derived D424N mutant[18], influencing a key residue in the transport mechanism we identified. We derived that MCT8 D424N is well-folded and still able to bind T4, but its transport efficacy is highly reduced due to an increased flexibility of the CTD, which prevents an efficient closure of the gate (Fig. 5).

In conclusion, in this work, combining structural findings with functional assays, we dissected the principles of binding and transport of thyroid hormones to MCTs and identified essential residues regulating access to two opposite membrane-separated compartments. In addition, our modular ALFA-tag fusion/NbALFA complex strategy allowed us to determine MCT8/10 structures of OFS, IFS, and pathogenic variants readily, without using specific anti-MCT8/10 antibodies. This opens the way to a faster determination of MCTs variants' architecture, and together with the WT structures, to build a structure-educated interpretation of pathogenic variants[7]. Taken together, our results contribute to further understanding of the principles and substrate specificity of MCTs and their mechanisms of transport.

Methods

Constructs

N-terminally FLAG-tagged pcDNA3-hMCT8 was previously generated[27]. A FLAG tag was subcloned at the N-terminus of the previously generated pcDNA3.1-MCT10 plasmid using HindIII and XbaI restriction sites after polymerase chain reaction (PCR) amplification of WT MCT10 cDNA using forward primers containing the FLAG tag sequence (Supplementary Fig. 9)[2]. We numbered the residues according to the short MCT8 isoform; to convert the number to the long MCT8 isoform (NM_006517.3), which has been used in the past to describe patient mutations and in homology models, 74 amino acids should be added (Supplementary Fig. 10). The position of the mutations is indicated using the NM_006517.3 reference sequence and uses +1 as the A of the ATG translation initiation codon of the long MCT8 isoform, with the initiation codon as codon 1. DNA sequencing confirmed the presence of the introduced mutations and the absence of unintended mutations.

For cryo-EM structural studies of MCT8, both in its unbound form and in complex with L-thyroxine (T4) or silychristin, an ALFA tag (SRLEEELRRRLTEP) was introduced at position P505. In the MCT8 D424N variant, the ALFA tag was placed at F512. For MCT10 bound to L-thyroxine, the tag was fused at P470 (Supplementary Fig. 10). The following C-terminal residues were deleted.

For MCT8 and MCT10 site-directed mutagenesis, Q5 DNA polymerase (NEB) and Hi-Fi DNA assembly (NEB) were used.

L-thyroxine (T4) uptake assay

HeLa cells were cultured in Dulbecco's Modified Eagle's Medium (Euroclone, ECB7501LX10) supplemented with 10% (v/v) heat-inactivated fetal bovine serum (Life Technologies, 10500064), 100 IU/ml penicillin−streptomycin (Euroclone, ECB3001D), and 2 mM L-glutamine (Euroclone, ECB3004D) at 37 °C under atmospheric O_2 and 5% CO_2.

HeLa cells were plated in 24-well plates at a density of 50,000 cells per well and allowed to adhere for at least 24 h. Cells were then transfected with MCT8 or MCT10 vectors (wild-type or mutants, see Supplementary Fig. 8) using Lipofectamine 2000 (Invitrogen, 11668019). The medium containing the transfection reagents was replaced with fresh medium 5 h post-transfection. The day after transfection, 10 µM L-thyroxine (T4) and/or 10 µM silychristin were added to the medium for 20 min. The wells were washed three times with phosphate-buffered saline buffer (PBS), and cells were fixed with 4% paraformaldehyde (PFA) for 10 min at room temperature. Cells were then washed three times for at least 5 min in PBS before blocking for 1 h at room temperature with PBS supplemented with 0.1% (v/v) Triton X-100 and 1% (v/v) donkey serum. After blocking, cells were incubated for 2 h at room temperature with primary antibodies diluted

in staining solution (PBS supplemented with 0.1% Triton X-100 and 1% donkey serum). The primary antibodies were mouse monoclonal anti-T4 (Santa Cruz, sc-52247, ICC 1:50), rabbit polyclonal anti-SLC16A2 (Sigma-Aldrich, HPA003353-100UL, ICC 1:200), and rabbit polyclonal anti-FLAG (Sigma-Aldrich, F7425-2MG, ICC 1:100).

The cells were then washed with PBS three times for 5 min, following incubation with Alexa Fluor™ Plus 647 Phalloidin (Thermo Scientific, A30107, ICC 1:400) and Hoechst 33342 (Sigma-Aldrich, B2261, 0.2 µg/ml) diluted in PBS for 30 min at room temperature. After incubation with the dyes, the cells were washed with PBS three times for 5 min, followed by incubation with secondary antibodies diluted in staining solution for 1 h at room temperature. The following fluorescence-conjugated secondary antibodies were used: Donkey anti-Rabbit IgG (H + L) Alexa Fluor 488 (Thermo Scientific, A21206, ICC 1:500) and Goat anti-Mouse IgG (H + L) Highly Cross-Adsorbed Alexa Fluor Plus 555 (Thermo Scientific, A32727, ICC 1:500). The cells were washed twice for 5 min with PBS. The cells were then mounted on glass coverslips using the DAKO Mounting Solution (Agilent DAKO, S302380-2).

Confocal microscopy analysis was performed using a Zeiss LSM980 point-scanning confocal microscope based on a Zeiss Observer7 inverted microscope. The images were acquired using a PlanApo 40X/1.4NA oil immersion objective with 488 and 561 nm laser lines. All image acquisition was performed using Zen Blue 3.7 software (Zeiss). The image analysis and quantification were carried out with the support of the Human Technopole Image Analysis Facility using Python pipelines. Each experiment was conducted at least in triplicate. For each replicate, fluorescence intensity was measured in grayscale levels from at least 100 randomly selected cells. An automatic custom Python pipeline was used to analyze the confocal images. Cells and nuclei were segmented with Cellpose[28] pretrained models using phalloidin and DAPI channels. The mean intensity of the T4 signal was calculated for single cells on the whole cell area, excluding the nucleus.

MCT8 and MCT10 purification

Expi293F™ cells (Thermo Fisher Scientific) were cultured in Dynamis™ AGT™ Medium (Thermo Fisher Scientific) supplemented with 1% (v/v) penicillin−streptomycin (Euroclone) and 4 mM stable glutamine (Euroclone) at 130 rpm, 8% CO_2, 37 °C, and 85% humidity. These cells were used to produce MCT10, MCT8, and all corresponding mutants. The cells were grown to a concentration of $2-3 \times 10^6$ cells/mL with a viability greater than 95%. The transfection was performed without a prior media change. For each litre of culture, 1.1 mg of DNA plasmid and 3 mg of polyethyleneimine (PEI Prime, Sigma-Aldrich) were pre-diluted separately in 25 mL of pre-warmed media before being combined. After incubating the plasmid-PEI mixture for 20 min at room temperature, the 50 mL complex was added dropwise to the cells. Protein expression was allowed to proceed for 72 h. The cells were then collected by centrifugation at $1000 \times g$ for 10 min.

The resulting pellet was resuspended in 10 mL of lysis buffer per 1 g of cell mass (25 mM HEPES), pH 7.5, 150 mM NaCl, 1.5% n-dodecyl-β-d-maltopyranoside (βDDM; Anatrace), supplemented with 10 µg/mL DNase I and 1x cOmplete™ EDTA-free protease inhibitor cocktail (Roche). Cell lysis and membrane solubilization were carried out using a Dounce homogenizer and incubated at 4 °C for 2 h. The soluble fraction was separated via centrifugation ($45,000 \times g$ for 1 h). The clarified lysate was then loaded onto 10 mL of M2 anti-FLAG affinity resin (Anti-FLAG® M2 affinity gel, Sigma-Aldrich), which had been pre-equilibrated with Buffer A (25 mM HEPES, pH 7.5, 150 mM NaCl, 0.04% βDDM). The mixture was gently stirred at 4 °C for 1 h, and the beads were collected by centrifugation at $1000 \times g$ for 10 min. The beads were transferred to a 100 mL EconoColumn (Bio-Rad) and washed with 5 column volumes (CV) of Buffer A. The elution was performed using 5 CV of Buffer A supplemented with 0.2 mg/mL FLAG peptide (Tebu Bio) to release the MCT8/10 proteins. All fractions were analyzed by SDS-

PAGE, and positive fractions were pooled and concentrated to 500 μL using a 100 kDa MW cut-off concentrator (Millipore). Final purification was performed by size-exclusion chromatography on a Superose 6 Increase 10/300 column (GE Healthcare) equilibrated in Buffer A. The fractions containing purified MCT8/10 were combined and concentrated to -1 mg/mL using a 100 kDa MW cut-off concentrator (Millipore), then aliquoted and flash-frozen for storage at −80 °C.

Western blot

After SDS-PAGE, the gels were transferred onto 0.2 μm nitrocellulose membranes using the Trans-Blot Turbo Transfer System (Bio-Rad). The membranes were blocked for 1 h in TBS buffer (200 mM NaCl, 20 mM TRIS, pH 7.5) supplemented with 0.1% Tween-20 (PanReac AppliChem) and 5% skim milk powder (Sigma-Aldrich) and incubated overnight at 4 °C with gentle agitation using the primary Anti-FLAG M2 antibody (Sigma-Aldrich, mouse, diluted 1:1000). The membranes were washed three times for 10 min in TBS containing 0.1% Tween-20 before incubating 1 h at room temperature with the HRP-conjugated Goat anti-Mouse IgG (H + L) secondary antibody (Invitrogen, diluted 1:10,000). Afterward, the membranes were washed three more times in TBS containing 0.1% Tween-20, and the blots were developed using the Clarity Western ECL Substrate (Bio-Rad) in a ChemiDoc system (Bio-Rad).

MCT8 and MCT10 cryo-EM studies

Single particle cryo-EM was used to ensure the correct folding of MCT8 and MCT10 stabilized in βDDM (Supplementary Fig. 1e, f). 2.5 μL of MCT8 and MCT10 at 4 mg/mL were vitrified in liquid ethane using a Vitrobot Mark IV (FEI). For MCT8, 26166 images were recorded on a Titan Krios G4 transmission electron microscope (Thermo Scientific) operated at 300 kV in EF-TEM mode, and for MCT10, 920 images were recorded on a Glacios transmission electron microscope operated at 200 kV. Both microscopes were equipped with a Falcon 4i (Thermo Scientific) direct electron detector and a Selectris X (Thermo Scientific) post-column energy filter with a slit width of 10 eV. 800,000 and 240,000 particles were picked to generate 2D class averages for MCT8 and MCT10, respectively, using cryoSPARC[29].

Purification of the anti-ALFA tag nanobody (NbALFA)

A 2xYT medium supplemented with 100 μg/mL ampicillin was inoculated with E. coli BL21 (DE3) transformed with pNT1440-$_{HIS-TEV}$NbALFA. The culture was grown at 37 °C at 200 rpm until OD600 = 0.6. $_{HIS-TEV}$NbALFA expression was induced by adding 0.55 mM IPTG while decreasing the temperature to 17.5 °C for 16 h. Cells were harvested by centrifugation at 4500 × g for 20 min at 4 °C. During purification, the sample was kept at 4 °C.

The cells were resuspended in cold lysis buffer (50 mM HEPES pH 8, 50 mM NaCl, 5 mM MgCl$_2$, and 1 tablet 50 mL^{-1} EDTA-free protease inhibitor, Roche) plus 0.5 mg/mL lysozyme and 0.1 mg/mL DNase I (Sigma) and stirred at room temperature for 20 min. Cells were lysed through three cycles on a CF1 Cell Disruptor at 20kpsi (Constant Systems). The cell lysate was centrifuged at 45,000 × g for 30 mi, and the insoluble material was collected. The pellet was washed and centrifuged twice with 25 mM HEPES pH 7.5, 150 mM NaCl, 1 M urea, and 1% Triton X-100 before solubilizing the inclusion bodies in 25 mM HEPES pH 7.5, 150 mM NaCl, and 6 M guanidine hydrochloride. $_{HIS-TEV}$NbALFA was refolded by an overnight dialysis in 25 mM HEPES, 150 mM NaCl, and 10 mM imidazole and clarified by centrifugation at 45,000 × g. The supernatant was incubated for 1 h with 10 mL of Ni Sepharose High Performance resin (Merck) pre-equilibrated with dialysis buffer. The slurry was washed with dialysis buffer supplemented with 50 mM imidazole before collecting the elution fraction by adding 500 mM imidazole.

The eluted $_{HIS-TEV}$NbALFA was supplemented with TEV$_{HIS}$ protease in a 1:10 ratio, 1 mM DTT, 0.5 mM EDTA, and incubated for 3 h at room temperature with mild shaking, followed by overnight dialysis in 25 mM HEPES and 150 mM NaCl. To remove uncleaved Nanobody and TEV$_{HIS}$, a reverse IMAC was performed, and the flow-through collected. The sample was then concentrated using an Amicon® Ultra (MWCO 3 kDa) up to 5 mL and injected on a Superdex75 16/600 PrepGrade column (Cytiva). The eluted sample was stored at −80 °C.

Sample preparation for cryo-EM structural studies

Purified MCT8/10 constructs bearing the ALFA-tag were incubated with a 3-fold molar excess of nanobody α-ALFA tag for 1 h at 4 °C with gentle shaking. A ten-fold excess (mg: mg) of Amphipols (PMAL-C8, Anatrace) was then added and incubated overnight. The detergent was removed by incubating the sample with Biobeads (Bio-Rad) for 2 h at 4 °C. Final polishing was achieved by injecting the sample onto a Superdex 200 10/300 column equilibrated with 25 mM HEPES, pH 7.5, and 150 mM NaCl. For vitrification, 2.5 μL of a 0.5 mg/mL sample, optionally supplemented with 20 μM T4 or 40 μM silychristin, was incubated for 10 s onto an R1.2/1.3 Quantifoil 200 mesh copper grid (Electron Microscopy Science) before vitrification in liquid ethane using a Vitrobot Mark IV (FEI).

Cryo-EM data collection

Data acquisition was performed on a Titan Krios G4 transmission electron microscope (Thermo Scientific) operated at 300 kV in EF-TEM mode and equipped with a Falcon 4i (Thermo Scientific) direct electron detector and a Selectris X (Thermo Scientific) post-column energy filter with a slit width of 10 eV. All datasets were collected using EPU automated acquisition software in electron counting mode at a nominal magnification of 165,000×, corresponding to a calibrated pixel size of 0.748 Å/pixel, and at a defocus range of −0.8 to −2.0 μm. The datasets were recorded in Electron Event Representation (EER) file format. A total of 44,327 movies were collected for MCT8 D424N, 36,940 for MCT8-silychristin, 41,224 for MCT8, 22,504 for MCT8-T4, and 36,610 for MCT10-T4. EER files were fractionated to achieve a dose of 1 e$^-$Å^{-2} per frame.

Cryo-EM data processing

The processing workflow is illustrated in Supplementary Fig. 2. EER movies were averaged using MotionCorr within Relion5[30,31], and the corrected micrographs were exported to cryoSPARC[29]. Contrast Transfer Function (CTF) parameters were calculated using Patch CTF estimation. For all datasets, -7–10 million particles were extracted and sorted through at least five iterations of 2D class average classifications, yielding about 500,000 to 800,000 particles. This particle stack was further classified through a series of Ab initio reconstructions (two or three classes), followed by non-uniform refinement and local refinement iterative cycles until resolution, B-factor, and Fourier space completeness ceased to improve. The resulting stack of -100,000–180,000 particles was imported into Relion5[30] for 3D Classification and Auto-refine with Blush. CTF refinement and Bayesian polishing were performed on the final particle stack, and amphipol densities were removed during post-processing using a mask generated from the PDB model.

Model building

For MCT8, an AlphaFold2 inward-facing model template was downloaded from UniProt (P36021). The outward-facing MCT10 template model was generated with Swiss-Model[19] using MCT1 (PDB ID: 7YR5)[25] as a template. For both MCT8 and MCT10, the models were rigid-body fitted into the cryo-EM maps and refined using Coot[32]. Further refinement was performed with iSOLDE[33] and Phenix[34]. Ligand restraints for T4 and silychristin were generated using Elbow. Additional information is available in Supplementary Table 1. Model analysis and visualization were performed in PyMol and ChimeraX[35,36]. Conservation analysis was performed with ConSurf[37]. In the MCT8 map, we initially

placed the ligand based on the density of the iodophenol rings, which is well-defined. We then modeled the amino acidic group based on the best geometrical parameters, and we were also guided by proximity with the highly conserved R371, which is likely to bind a carboxylate, rather than an amino group bearing the same charge (PDB ID: 7YR5[25]). However, we do not exclude that the ligand may be flexible and experiment local conformational changes. The MCT10 map in the IFS (going to release the ligand) presents a lower resolution, and to model T4, we started with T4 coordinates as bound to MCT8, then again used multiple thresholds and produced the best ligand fit.

Microscale thermophoresis

MST MCT8/10 (WT and mutants) were tested for interaction with ligands of interest using a Monolith instrument (Nanotemper), using LabelFree standard capillaries, monitoring intrinsic protein fluorescence (Supplementary Fig. 2b). All the ligands (T4, T3, TRIAC, silychristin) were resuspended in DMSO, and a 16-point dilution series was prepared over specific concentration range in the final assay buffer (25 mM HEPES pH 7.5, 150 mM NaCl, 0.04 % βDDM and 5% DMSO). Binding reactions were prepared by adding protein at a 50 nM concentration, leaving the mix for 10 min at room temperature. Since the addition of ligands induced a decrease in fluorescence signal, an SDS-denaturation (SD) test was performed, following the manufacturer's protocol, to ensure fluorescence changes were not caused by non-specific effects. Since in denaturing conditions the fluorescence signal of the ligand-containing points was unchanged with respect to that of ligand-free points, we concluded that initial fluorescence intensities might be used to ascertain ligand binding and for equilibrium dissociation constants (K_d) calculation. Measurements were conducted with 100% excitation power and MST power set to high, initial fluorescence data were analyzed, and K_d values were obtained using GraphPad Prism. For the competitive binding experiments, MCT8/10 was incubated overnight with either 100 μM T4 or 50 μM Silychristin. All experiments were performed in biological triplicate.

Isothermal titration calorimetry (ITC)

The thermodynamics of the MCT8-silychristin interaction were determined using ITC on a MicroCal PEAQ ITC instrument (Malvern Panalytical). A 10 μM MCT8 solution was titrated with silychristin (100 μM) using injections of 2 μL. Protein and ligand were prepared and diluted to be in the same final buffer (25 mM HEPES pH 7.5, 150 mM NaCl, 0.04 % βDDM). Calorimetric data were analyzed with the instrument software, providing thermodynamic fitting parameters such as the reaction enthalpy change (ΔH, cal mol^{-1}) and the binding constant (K_a, M^{-1}). The reaction entropy (ΔS) was derived using the equations $\Delta G = -RT\ln K_a$ (where $R = 1.9872$ cal mol^{-1} K^{-1}, and $T = 298$ K) and $\Delta G = \Delta H - T\Delta S$. The best fit was determined using the statistical goodness-of-fit parameter. The measurement was repeated three times, and after each run, the sample was collected and injected onto a Superose 6 10/300 column to assess that the sample was monodisperse.

Reporting summary

Further information on research design is available in the Nature Portfolio Reporting Summary linked to this article.

Data availability

Atomic coordinates have been deposited in the Protein Data Bank (PDB) and Electron microscopy Data Bank under accession codes 9GSZ/EMD-51559 (Human monocarboxylate 10 bound to L-thyroxine), 9GF8/EMD-51311 (Human Monocarboxylate Transporter 8), 9FOT/EMD-50629 (Human monocarboxylate transporter 8 bound to silychristin), 9FKN/EMD-50523 (Human monocarboxylate transporter 8 bound to L-thyroxine), 9GV5, EMD-51624 (Human monocarboxylate

transporter 8 D424N mutant). In this manuscript, we referred to the following PDB coordinates: 6LZ0, 7DSQ, 7YR5. Source data are provided with this paper.

References

1. Friesema, E. C. H. et al. Identification of monocarboxylate transporter 8 as a specific thyroid hormone transporter. *J. Biol. Chem.* **278**, 40128–40135 (2003).
2. Friesema, E. C. H. et al. Effective cellular uptake and efflux of thyroid hormone by human monocarboxylate transporter 10. *Mol. Endocrinol.* **22**, 1357–1369 (2008).
3. Brent, G. A. Mechanisms of thyroid hormone action. *J. Clin. Investig.* **122**, 3035–3043 (2012).
4. Groeneweg, S., van Geest, F. S., Peeters, R. P., Heuer, H. & Visser, W. E. Thyroid hormone transporters. *Endocr. Rev.* **41**, bnz008 (2020).
5. Bernal, J., Guadaño-Ferraz, A. & Morte, B. Thyroid hormone transporters–functions and clinical implications. *Nat. Rev. Endocrinol.* **11**, 406–417 (2015).
6. Groeneweg, S. et al. Disease characteristics of MCT8 deficiency: an international, retrospective, multicentre cohort study. *Lancet Diabetes Endocrinol.* **8**, 594–605 (2020).
7. Groeneweg, S. et al. Mapping variants in thyroid hormone transporter MCT8 to disease severity by genomic, phenotypic, functional, structural and deep learning integration. *Nat. Commun.* **16**, 2479 (2025).
8. Groeneweg, S. et al. Effectiveness and safety of the tri-iodothyronine analogue Triac in children and adults with MCT8 deficiency: an international, single-arm, open-label, phase 2 trial. *Lancet Diabetes Endocrinol.* **7**, 695–706 (2019).
9. van Geest, F. S. et al. Long-term efficacy of T3 analogue Triac in children and adults with MCT8 deficiency: a real-life retrospective cohort study. *J. Clin. Endocrinol. Metab.* **107**, e1136–e1147 (2022).
10. Felmlee, M. A., Jones, R. S., Rodriguez-Cruz, V., Follman, K. E. & Morris, M. E. Monocarboxylate transporters (SLC16): function, regulation, and role in health and disease. *Pharmacol. Rev.* **72**, 466–485 (2020).
11. Kinne, A. et al. Essential molecular determinants for thyroid hormone transport and first structural implications for monocarboxylate transporter 8. *J. Biol. Chem.* **285**, 28054–28063 (2010).
12. Johannes, J. et al. Silychristin, a flavonolignan derived from the milk thistle, is a potent inhibitor of the thyroid hormone transporter MCT8. *Endocrinology* **157**, 1694–1701 (2016).
13. Groeneweg, S. et al. Outward-open model of thyroid hormone transporter monocarboxylate transporter 8 provides novel structural and functional insights. *Endocrinology* **158**, 3292–3306 (2017).
14. Yan, N. Structural biology of the major facilitator superfamily transporters. *Annu. Rev. Biophys.* **44**, 257–283 (2015).
15. Halestrap, A. P. The SLC16 gene family—structure, role and regulation in health and disease. *Mol. Asp. Med.* **34**, 337–349 (2013).
16. Quistgaard, E. M., Löw, C., Guettou, F. & Nordlund, P. Understanding transport by the major facilitator superfamily (MFS): structures pave the way. *Nat. Rev. Mol. Cell Biol.* **17**, 123–132 (2016).
17. Groeneweg, S. et al. The role of Arg445 and Asp498 in the human thyroid hormone transporter MCT8. *Endocrinology* **155**, 618–626 (2014).
18. Islam, M. S. et al. Functional analysis of monocarboxylate transporter 8 mutations in Japanese Allan-Herndon-Dudley syndrome patients. *Endocr. J.* **66**, 19–29 (2019).
19. Waterhouse, A. et al. SWISS-MODEL: homology modelling of protein structures and complexes. *Nucleic Acids Res.* **46**, W296–W303 (2018).
20. Johannes, J. et al. Few amino acid exchanges expand the substrate spectrum of monocarboxylate transporter 10. *Mol. Endocrinol.* **30**, 796–808 (2016).

21. Groeneweg, S. et al. In vitro characterization of human, mouse, and zebrafish MCT8 orthologues. *Thyroid* **29**, 1499–1510 (2019).

22. Kersseboom, S. et al. In vitro and mouse studies supporting therapeutic utility of triiodothyroacetic acid in MCT8 deficiency. *Mol. Endocrinol.* **28**, 1961–1970 (2014).

23. Groeneweg, S. et al. Identification of iodotyrosines as novel substrates for the thyroid hormone transporter MCT8. *Thyroid* **34**, 931–941 (2024).

24. Groeneweg, S., Lima de Souza, E. C., Visser, W. E., Peeters, R. P. & Visser, T. J. Importance of His192 in the human thyroid hormone transporter MCT8 for substrate recognition. *Endocrinology* **154**, 2525–2532 (2013).

25. Wang, N. et al. Structural basis of human monocarboxylate transporter 1 inhibition by anti-cancer drug candidates. *Cell* **184**, 370–383.e13 (2021).

26. Yan, R. et al. Mechanism of substrate transport and inhibition of the human LAT1-4F2hc amino acid transporter. *Cell Discov.* **7**, 16 (2021).

27. Groeneweg, S. et al. Insights into the mechanism of MCT8 oligomerization. *J. Endocr. Soc.* **4**, bvaa080 (2020).

28. Pachitariu, M. & Stringer, C. Cellpose 2.0: how to train your own model. *Nat. Methods* **19**, 1634–1641 (2022).

29. Punjani, A., Rubinstein, J. L., Fleet, D. J. & Brubaker, M. A. cryoSPARC: algorithms for rapid unsupervised cryo-EM structure determination. *Nat. Methods* **14**, 290–296 (2017).

30. Burt, A. et al. An image processing pipeline for electron cryotomography in RELION-5. *FEBS Open Bio.* **14**, 1788–1804 (2024).

31. Zheng, S. Q. et al. MotionCor2: anisotropic correction of beam-induced motion for improved cryo-electron microscopy. *Nat. Methods* **14**, 331–332 (2017).

32. Emsley, P. & Cowtan, K. Coot: model-building tools for molecular graphics. *Acta Crystallogr. D Biol. Crystallogr.* **60**, 2126–2132 (2004).

33. Croll, T. I. ISOLDE: a physically realistic environment for model building into low-resolution electron-density maps. *Acta Crystallogr. Sect. Struct. Biol.* **74**, 519–530 (2018).

34. Afonine, P. V. et al. Real-space refinement in PHENIX for cryo-EM and crystallography. *Acta Crystallogr. Sect. Struct. Biol.* **74**, 531–544 (2018).

35. Meng, E. C. et al. UCSF ChimeraX: tools for structure building and analysis. *Protein Sci.* **32**, e4792 (2023).

36. Schrödinger, L. L. C. The PyMOL Molecular Graphics System, Version 1.8. Available from: http://www.pymol.org/pymol (2015).

37. Ashkenazy, H. et al. ConSurf 2016: an improved methodology to estimate and visualize evolutionary conservation in macromolecules. *Nucleic Acids Res.* **44**, W344–W350 (2016).

Acknowledgements

Author contributions

M.T. performed cloning, biochemistry, biophysics, EM data collection and processing, model building, and structural analysis. G.T. performed transport and inhibition experiments in cells and relative data analysis. I.B. performed preliminary biochemistry and structural analysis of MCT8. F.M. performed cloning, biochemistry, and biophysics experiments, assisted by M.T. S.P. provided help with biophysics data collection and analysis. M.F. and C.S. performed cloning. S.G., F.S.v.G., W.E.V., F.C., M.T., and G.T. provided interpretation to the data. F.C., W.E.V., and M.T. wrote the draft manuscript. All authors assisted with manuscript preparation.

Competing interests

The authors declare no competing interests.

Additional information

Supplementary information The online version contains supplementary material available at https://doi.org/10.1038/s41467-025-59751-w.

Correspondence and requests for materials should be addressed to W. Edward Visser or Francesca Coscia.

Peer review information *Nature Communications* thanks Derek Claxton and Yongchan Lee for their contribution to the peer review of this work. A peer review file is available.

Reprints and permissions information is available at http://www.nature.com/reprints

Publisher's note Springer Nature remains neutral with regard to jurisdictional claims in published maps and institutional affiliations.